Molecular dynamics simulations of wetting behaviors of droplets on surfaces with different rough structures

Yanling Chen[a], Liang Guo[a*], Wanchen Sun[a], Ningning Cai[b], Yuying Yan[c]

[a] *State Key Laboratory of Automotive Simulation and Control, Jilin University, Changchun 130025, China*

[b] *School of Business and Management, Jilin University, Changchun 130012, China*

[c] *Faculty of Engineering, University of Nottingham, Nottingham NG7 2RD, UK*

Abstract: Aiming at the wall-wetting problem in internal combustion engines, to actively control the behaviors of fuel droplets after hitting the walls, the molecular dynamics method is used to investigate the effects of surface wettability and rough structure on the static and dynamic wetting behaviors of the droplets. The results show that the droplet diameter has little influence on the intrinsic contact angle. With the decrease of the solid-liquid interaction coefficient, the interaction between the wall and the droplet is weakened and the wetting state changes from the Wenzel state to the Cassie state, resulting in an increase in the apparent contact angle. As the ratio of the solid-liquid contact area to the composite contact area decreases, it is easier for the droplet to reach the Cassie state. Compared with the smooth surfaces, the rough structures of the surfaces have an inhibitory effect on the spreading of the droplets, so the apparent contact angles of the droplets on the surfaces with different rough structures are larger than their intrinsic contact angles on the smooth surfaces. The secondary boss-shaped structures can significantly enhance the surface oleophobicity. In addition, with the decrease of the solid-

---

[*] Corresponding author.
E-mail address: liangguo@jlu.edu.cn (L. Guo).

liquid interaction coefficient, the contact angle hysteresis of the droplets on different surfaces reduces. Compared with the Wenzel state, the droplet in the Cassie state has a smaller contact area with the surface, which makes the interaction between the wall and the droplet weaker, leading to a decrease in the contact angle hysteresis.

Keywords: Droplet; Wettability; Rough structure; Static contact angle; Contact angle hysteresis; Molecular dynamics

1. Introduction

Advanced combustion modes such as homogeneous charge compression ignition (HCCI), premixed charge compression ignition (PCCI), reaction controlled compression ignition (RCCI) and low temperature combustion (LTC) play an important role in improving combustion efficiency and reducing pollutant emissions of internal combustion engines (Gordon et al., 2020; Sankaralingam et al., 2022; Agarwal et al., 2017; Krishnamoorthi et al., 2019). However, premixed compression ignition modes such as HCCI and PCCI often use early injection, multiple injections and high-pressure injection to improve the atomization quality (Mathivanan et al., 2016; Liang et al., 2019; Lee et al., 2015). Due to the low temperature and gas density in the cylinder at the early injection timing, the wall-wetting phenomenon is inevitable (Bendu and Murugan, 2014). Especially when the engine is cold started, the wall-wetting problem is more obvious. Spray-wall impingement can cause an increase in soot particles and unburned hydrocarbons. Therefore, it is necessary to deeply study the effects of wall properties on the development processes of wall-impinging fuels to achieve active control of the wall-wetting problem.

As the applications of the technologies of drag reduction (Ou et al., 2004; Taghvaei et al., 2017), oil/water separation (Saleh and Baig, 2019), self-cleaning (Bhushan et al., 2009; Li et al., 2018), anti-icing (Farhadi et al., 2011; Qi et al., 2020) and anti-corrosion (Qian et al., 2017; Xin et al., 2021), the interest in wettability studies has been rising. The wettability is related to the morphologies and chemical compositions of the solid surfaces (Yong et al., 2015; Kim et al., 2018; Song et al., 2015). The surfaces with specific wettability can be prepared with different methods, such as mechanical treatment, chemical etching, plasma spraying and particle deposition, etc. Numerous experimental studies have been conducted on the influence of the wettability and textures of the solid surfaces on the static behaviors, dynamic behaviors (Yoshimitsu et al., 2002; Martines et al., 2005; Yao et al., 2020) and evaporation characteristics (Lee et al., 2012; Yu et al., 2015; Guo et al., 2022; Chen et al., 2023) of the droplets.

In addition, different wetting models have been proposed. The equilibrium contact angle (CA) of the droplet on a flat homogeneous surface, θ_Y, is obtained by Young equation (Young, 1805). The expression of Young equation is as follows:

$$\cos\theta_\mathrm{Y} = \frac{\gamma_\mathrm{sv} - \gamma_\mathrm{sl}}{\gamma_\mathrm{lv}} \tag{1}$$

Where, γ_sv, γ_sl, and γ_lv are interfacial tensions per unit length of the solid-vapor, solid-liquid and liquid-vapor interfaces, respectively.

Considering that the actual surface has the rough structures, the CA of the droplet on a rough surface is called the apparent CA. The Young equation has been modified by Wenzel (1936), Cassie and Baxter (1944), respectively. The Wenzel equation is expressed as follows:

$$\cos\theta_\mathrm{W} = r_\mathrm{s}\frac{\gamma_\mathrm{sv} - \gamma_\mathrm{sl}}{\gamma_\mathrm{lv}} = r_\mathrm{s}\cos\theta_\mathrm{Y} \tag{2}$$

Where, r_s is the roughness factor. The value of r_s is the ratio of the real area of a solid surface in contact with the droplet to its projection onto the horizontal plane.

In the Cassie-Baxter theory, the droplet does not wet the inside of the grooves on the rough surface and the grooves are filled with air. The lower part of the droplet is in contact with both a solid surface and air. As a result, a composite contact surface consisting of a solid-liquid contact surface and a liquid-vapor contact surface is formed. The Cassie-Baxter equation is expressed as follows:

$$\cos\theta_{\mathrm{C}} = f_1 \frac{\gamma_{\mathrm{sv}} - \gamma_{\mathrm{sl}}}{\gamma_{\mathrm{lv}}} - f_2 = f_1 \cos\theta_{\mathrm{Y}} - f_2 \tag{3}$$

Where, f_1 is the ratio of the solid-liquid contact area to the composite contact area. f_2 is the ratio of the liquid-vapor contact area to the composite contact area. Also, $f_1 + f_2 = 1$.

Due to the limitation of experimental conditions, it is difficult to measure some microscopic processes with experimental methods. Numerical simulation methods are widely used. The thicknesses of the liquid-solid interface and the liquid-vapor interface are usually about a few nanometers. The heat and mass transfer between the solid, liquid and vapor phases are carried out by atoms and molecules as individuals. Therefore, it is particularly important to use a discrete method to conduct related studies, and the molecular dynamics (MD) method is a good choice. In the research field of wettability, MD simulation makes it possible to investigate the wetting behaviors and microscopic mechanisms of the droplets on different surfaces. Guo and Fang (2005) studied the CAs of argon droplets on a solid substrate. They found the influence of the droplet size on the CA was related to the interaction between the liquid molecules and the solid substrate. The CA reduced with the decreasing droplet size for larger interaction between the liquid molecules and the solid substrate, and vice versa. Burt et al. (2016) simulated the wetting behaviors of ionic-liquid droplets on graphene sheets. They found that the droplet size had no significant effect on the CA at low graphene interaction potential. When increasing the surface interaction potential toward actual graphene, the spreading rate and extent of the droplets were influenced by the droplet size. Many scholars have carried out simulation studies on water molecules and compared the models of water such as TIP3P, TIP4P, TIP5P, SPC and SPC/E (Zielkiewicz, 2005). Chen et al. (2014) studied the wetting behaviors of water droplets on flat and pillar polytetrafluorethylene surfaces. They found that the cutoff of the Lennard-Jones potential had a large effect on the CA.

There are many MD simulation studies on the static and dynamic wetting behaviors of water droplets on the surfaces with different microstructures. Ambrosia et al. (2013) pointed out that the wetting states of water droplets on the surfaces with pillars included the Wenzel state and the Cassie state. Niu and Tang (2014) also conducted simulation studies on the behaviors of water droplets on the surfaces with pillar-type nanostructures and found that the wetting state of the droplet depended on the pillar height and the pillar surface fraction. Chen et al. (2014) studied the wetting behaviors of water droplets on the nanostructured pillar surfaces. They proposed the equilibrium states could be classified into four categories: the Wenzel, the metastable Cassie, the globally steady Cassie and the Cross state. In addition, the dual structures (Kwon et al., 2020) can make the surface more hydrophobic compared to the single structures. Zhang et al. (2016) analyzed the wettability of water droplets on the gold surfaces corrugated with spherical cavities and found that the CA varied from a hydrophilic (69°) to a hydrophobic value (>109°) with increasing depth of the cavities. Hong et al. (2009) simulated the static and dynamic CAs of water droplets on the solid surfaces using the method of MD. They found that as the characteristic energy of the solid surface increased, the static CA decreased and the CAH increased. Jeong et al. (2012) found that the CAH of water droplets on the surfaces with pillar-type nanostructures depended on the dynamic behaviors of the droplet under an external force. Similarly, Koishi et al. (2011) measured the CAH of water droplets on nanopillared surfaces. The results showed that the CAH for the droplet in the Wenzel state was larger than that in the Cassie state. In addition to exploring the effects of the droplet size, solid-liquid interaction coefficient and rough structure on the wetting states and CAs, many scholars have proposed some new methods for determining the CA suitable for MD simulations to improve the reliability and accuracy of the CA calculation results (Khalkhali et al., 2017; Ravipati et al., 2018; Abramov and Iglauer, 2019).

A lot of studies on the wetting processes of the droplets on different surfaces have been conducted. However, there are few studies on the wetting behaviors of alkane nanodroplets. Aiming at the wall-wetting problem in internal combustion engines, to actively control the development behaviors of the wall-impinging droplets, the molecular dynamics method is used to simulate the static and dynamic wetting behaviors of nano-scale droplets on the surfaces with different rough structures under the conditions of different solid-liquid interaction coefficients. The influence of the solid-liquid interaction coefficient and rough structure on the apparent CA and CAH of the alkane droplets are investigated. This study provides a theoretical foundation for guiding the design, choice, optimization and fabrication of combustion chamber surfaces in internal combustion engines to satisfy practical operating conditions.

2. Simulation method

2.1. The establishment of the simulation system

Molecular dynamics simulation is performed using the LAMMPS (Large-scale Atomic/Molecular Massively Parallel Simulator) software (Plimpton, 1995). For the study of the effects of the droplet size and cutoff radius on the static wetting behaviors of the droplets on the smooth surfaces, a simulation system with the three dimensions of 480 Å × 480 Å × 200 Å in the *x*, *y* and *z* directions is built. For the study of the static and dynamic wetting characteristics of the droplets on the surfaces with different rough structures, considering that a lateral force needs to be applied to the droplets, the three dimensions of the simulation system are determined to be 720 Å × 480 Å × 200 Å. A spherical region for the addition of droplet molecules is defined in the simulation system. The droplet is composed of n-hexadecane molecules in a body-centered cubic lattice structure. The n-hexadecane molecules are initially distributed with a density close to the liquid density (0.773 g/cm^3). To eliminate the influence of the initial configuration of the droplets, the process of the energy minimization is performed. The initial velocity of n-hexadecane molecules is determined by a random number generator. To avoid the lateral movement of the droplet due to accidental factors, the *x*-coordinate, *y*-coordinate and *z*-coordinate of the mass centroid (COM) of the droplet are fixed. The solid wall consists of aluminum atoms in a face-centered cubic lattice structure with a lattice constant is 4.0495 Å. The initial distance between the bottom of the droplet and the top of the wall is 20 Å. In this study, five kinds of surfaces are studied, which are smooth surface (SS), boss-shaped surface, pit-shaped surface (PS), grid-shaped surface (GS) and secondary boss-shaped surface (DS). Schematic diagrams of different surfaces are shown in Fig. 1. To describe the morphologies of the rough surfaces, the lattice length of the aluminum atom is defined as L. For the BS (PS), the length, width and height of each boss (pit) are 2L, and the distance between two adjacent bosses (pits) is 2L. For the GS, the length, width and height of each pit are 2L. For the DS, the length, width and height of the bottom boss are 2L, and the distance between two adjacent bottom bosses is 2L. The length, width and height of the upper boss are L. Taking a droplet on a smooth surface as an example, the initial configurations of the simulation systems with different sizes are shown in Fig. 2.

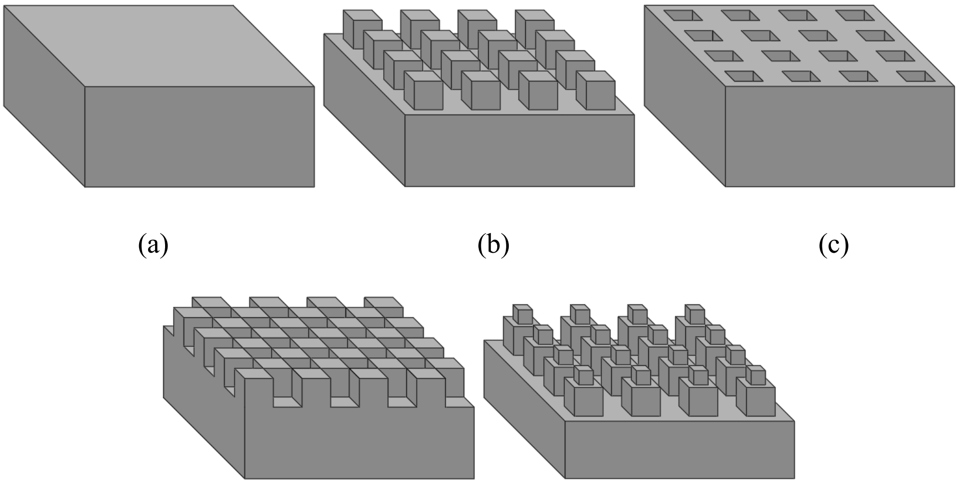

(a) (b) (c)

(d) (e)

Fig. 1. Schematic diagrams of (a) SS, (b) BS, (c) PS, (d) GS and (e) DS.

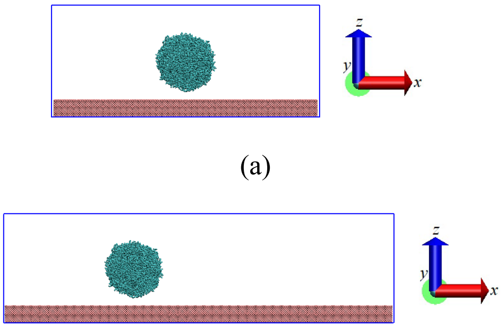

(a)

(b)

Fig. 2. Initial configurations of the simulation systems with the three dimensions of (a) 480 Å × 480 Å × 200 Å and (b) 720 Å × 480 Å × 200 Å.

2.2. Selection of potential energy model

Because the n-hexadecane molecule contains many atoms, to simplify the calculations, a joint atomic model is used (Bai et al., 2017), as shown in Fig. 3. Methyl (CH_3) and methylene (CH_2) are regarded as independent atoms, and their relative atomic masses are 15.0345 g/mol and 14.0266 g/mol, respectively. The simplified force field obtained is called the joint atomic force field. The chain-like property of n-hexadecane molecules will not be destroyed with the joint atomic force field.

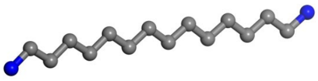

Fig. 3. Joint atomic model of n-hexadecane molecule.

The potential energy of n-hexadecane molecular system includes bonded and non-bonded potentials. The bonded potential includes bond length stretching potential, bond angle bending potential and dihedral angle twisting potential. The non-bonded potential is described by the 12-6 Lennard-Jones (L-J) potential. The potential energy function of n-hexadecane molecules is expressed as follows:

$$U^{\mathrm{tot}}=U^{\mathrm{NB}}+U^{\mathrm{B}}=\sum_{i=1}^{N}\sum_{j>1}^{N}4\varepsilon_{ij}\left[\left(\frac{\sigma_{ij}}{r_{ij}}\right)^{12}-\left(\frac{\sigma_{ij}}{r_{ij}}\right)^{6}\right]+\sum_{\mathrm{bonds}}\frac{1}{2}k_r(r-r_0)^2+\sum_{\mathrm{angles}}\frac{1}{2}k_\theta(\theta-\theta_0)^2+ \sum_{\mathrm{dihedrals}}\frac{1}{2}[k_1(1+\cos\alpha)+k_2(1-\cos2\alpha)+k_3(1+\cos3\alpha)+k_4(1-\cos4\alpha)] \quad (1)$$

Where, U^{tot} is the total potential, U^{NB} is the non-bonded potential and U^{B} is the bonded potential. N is the number of n-hexadecane molecules. ε_{ij} and σ_{ij} are the energy parameter and size parameter of the L-J potential between two non-bonded virtual atoms in molecules i and j. r_{ij} is the distance between two non-bonded virtual atoms in molecules i and j. k_r is the bond constant. r and r_0 are the actual bond length and equilibrium bond length between two covalently bonded virtual atoms. k_θ is the angle constant. θ and θ_0 are the actual angle and equilibrium angle between three covalently bonded virtual atoms. k_1, k_2, k_3 and k_4 are the dihedral angle constants. α is the dihedral angle.

The interaction parameters of bond length, bond angle and dihedral angle are shown in Tables 1, 2 and 3 (Bai et al., 2017).

Table 1. Interaction parameters of bond length.

Bond length	k_r/kJ·mol^{-1}·Å^{-2}	r_0/Å
CH_3-CH_2	1090.98	1.6100
CH_2-CH_2	813.43	1.6100

Table 2. Interaction parameters of bond angle.

Bond angle	θ_0/°	k_θ/kJ·mol^{-1}·rad^{-2}
CH_3-CH_2-CH_2	104.8	113.6
CH_2-CH_2-CH_2	102.2	93.6

Table 3. Interaction parameters of dihedral angle.

Dihedral angle	k_1/kJ·mol^{-1}	k_2/kJ·mol^{-1}	k_3/kJ·mol^{-1}	k_4/kJ·mol^{-1}
CH_3-CH_2-CH_2-CH_2	-3.4	1.25	0.3	0
CH_2-CH_2-CH_2-CH_2	-3.4	1.25	0.3	0

The energy and size parameters of the L-J potential between two non-bonded virtual atoms in the droplet molecules are shown in Table 4 (Bai et al., 2017).

Table 4. Energy and size parameters of L-J potential in the droplet molecules.

Atom group	ε_i/kJ·mol^{-1}	σ_i/Å
CH_3	0.7315	3.9050
CH_2	0.4932	3.9050

The potential between the wall atoms is described by the EAM potential function. The energy and size parameters of the L-J potential between virtual atoms and wall atoms can be calculated by using Lorentz–Bertholet mixing rule:

$$\varepsilon_{\mathrm{sl}}=\sqrt{\varepsilon_{\mathrm{ss}}\varepsilon_{\mathrm{ll}}} \tag{2}$$

$$\sigma_{\mathrm{sl}}=\frac{\sigma_{\mathrm{ss}}+\sigma_{\mathrm{ll}}}{2} \tag{3}$$

Where, $\varepsilon_{\mathrm{sl}}$, $\varepsilon_{\mathrm{ss}}$ and $\varepsilon_{\mathrm{ll}}$ are the energy parameters of the L-J potential between the droplet atoms and the wall atoms, between the wall atoms and between the droplet atoms. σ_{sl}, σ_{ss} and σ_{ll} are the size parameters of the L-J potential between the droplet atoms and the wall atoms, between the wall atoms and between the droplet atoms. The energy and size parameters of the L-J potential between different virtual atoms in the droplets are also obtained by the mixing rule. The interaction strength between the wall and the droplet can be changed by adjusting the energy parameters between the wall atoms and the droplet atoms. Therefore, the wettability can be changed by adjusting the interaction strength between the wall and the droplet. The energy parameter used to adjust the energy relationship between the wall atoms and the droplet atoms is called solid-liquid interaction coefficient. Four typical solid-liquid interaction coefficients are selected for subsequent calculations, which are represented by ε_1, ε_2, ε_3 and ε_4 in turn. The values of the four solid-liquid interaction coefficients can be found in Table 5.

Table 5. Solid-liquid interaction coefficients.

	ε_1/kJ·mol^{-1}	ε_2/kJ·mol^{-1}	ε_3/kJ·mol^{-1}	ε_4/kJ·mol^{-1}
$\varepsilon_{\mathrm{CH_3\text{-}Al}}$	0.5908	0.4178	0.2954	0.2089
$\varepsilon_{\mathrm{CH_2\text{-}Al}}$	0.4851	0.3431	0.2426	0.1716

2.3. Simulation details

In the simulations, periodic boundary condition is used in the *x* and *y* directions, while fixed boundary condition is applied in the *z* direction. Besides, a reflecting wall is adopted. For the simulations of the static wetting behaviors of the droplets on different surfaces, the *x*-coordinates and *y*-coordinates of the mass centroids of the droplets are controlled to be 0 to avoid the lateral movements of the droplets. The time step of the simulations is set to 1 fs and the duration is 2 ns. A run of the first 1 ns is used to ensure system equilibrium, and the simulation results from 1 ns to 2 ns are used for statistical analysis.

For the study relating to the effects of the rough structure on the dynamic wetting processes of the droplets, when the simulation mentioned above runs for 2 ns, an external force in the positive *x* direction is applied to the droplet in an equilibrium state. Under the same solid-liquid interaction coefficient, to ensure that all droplet atoms have the same acceleration, a constant external force is proportional to the mass of atoms CH_3 and CH_2. As the solid-liquid interaction coefficient decreases, the external force applied to a droplet reduces. The time step is set to 1 fs and the duration is 0.5 ns.

The NVT ensemble is used during the simulations with a constant number of atoms (N), fixed volume (V) and fixed temperature (T). The Nosé-Hoover thermostat is used to control the droplet temperature near 300.15 K. The velocity-Verlet algorithm is used to solve the motions of all particles.

2.4. Data processing

The static CAs of the droplets on different surfaces can be obtained by processing the two-dimensional density profiles obtained from the simulations. The method for obtaining the density profiles is as follows. During the simulations, the simulation system is divided into some concentric rings. The axes of the rings are along the *z*-axis direction, and the thickness of each ring in the *x*-*y* plane is 2 Å. Subsequently, the rings are cut at equal intervals along the *z*-axis from 0 Å to 200 Å. Each bin has a height of 2 Å in the *z*-axis direction. The density in each bin is calculated to obtain a two-dimensional density profile.

The method of obtaining the dynamic CAs is different from the method of obtaining the static

CAs. The specific method for obtaining dynamic CAs is as follows. The three-dimensional hexahedron computational domain is divided into some cubic bins with a side length of 4 Å. The distributions of the droplet atoms are determined according to the coordinates of each droplet atom obtained from the simulations. To make the density field smooth, combined with a smoothing procedure for two-dimensional density field (Bonometti and Magnaudet, 2007), the weighted average density ($\tilde{\rho}$) of a given grid point (m, n, p) and its surrounding grid points in the 3D computational domain is calculated as the density (ρ) of a given grid point by the following equation.

$$\tilde{\rho}_{m,n,p}=\frac{3}{4}\bar{\rho}_{m,n,p}+\frac{1}{24}\left(\bar{\rho}_{m+1,n,p}+\bar{\rho}_{m\text{-}1,n,p}+\bar{\rho}_{m,n+1,p}+\bar{\rho}_{m,n\text{-}1,p}+\bar{\rho}_{m,n,p+1}+\bar{\rho}_{m,n,p\text{-}1}\right) \tag{4}$$

Where, $\bar{\rho}$ is the average value of the density of the grid point.

Subsequently, a two-dimensional density profile in the *x*-*z* plane is obtained.

The CAs of the droplets on different surfaces are calculated using the isodensity circle fitting method. The 0.3865 g/cm^3 isodensity line is selected as the contour line of the droplet. For fitting the contour line of the droplet, only points with a distance greater than 4 Å against the solid surface are considered to avoid density fluctuation at the wall-droplet interface.

3. Results and Discussion

3.1. Analysis of the effects of the diameter on the static wetting behaviors of the droplets

The wetting processes of the droplets on the walls are scale-dependent. To explore the influence of the droplet size on the simulation results, at a solid-liquid interaction coefficient of ε_2, the static wetting behaviors of the droplets with diameters of 80 Å, 90 Å, 100 Å, 110 Å and 120 Å on the smooth surfaces are simulated. The numbers of n-hexadecane molecules contained in the above droplets are 544, 789, 1074, 1423 and 1864, respectively. The cutoff radius is 10 Å. Under a solid-liquid interaction coefficient of ε_2, the snapshots and density profiles of the droplets with different diameters on the smooth surfaces at 2 ns are shown in Fig. 4 and Fig. 5, respectively.

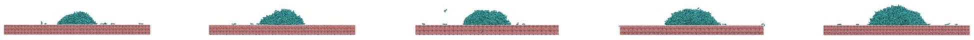

(a) (b) (c) (d) (e)

Fig. 4. Snapshots of the droplets with diameters of (a) 80 Å, (b) 90 Å, (c) 100 Å, (d) 110 Å and (e) 120 Å.

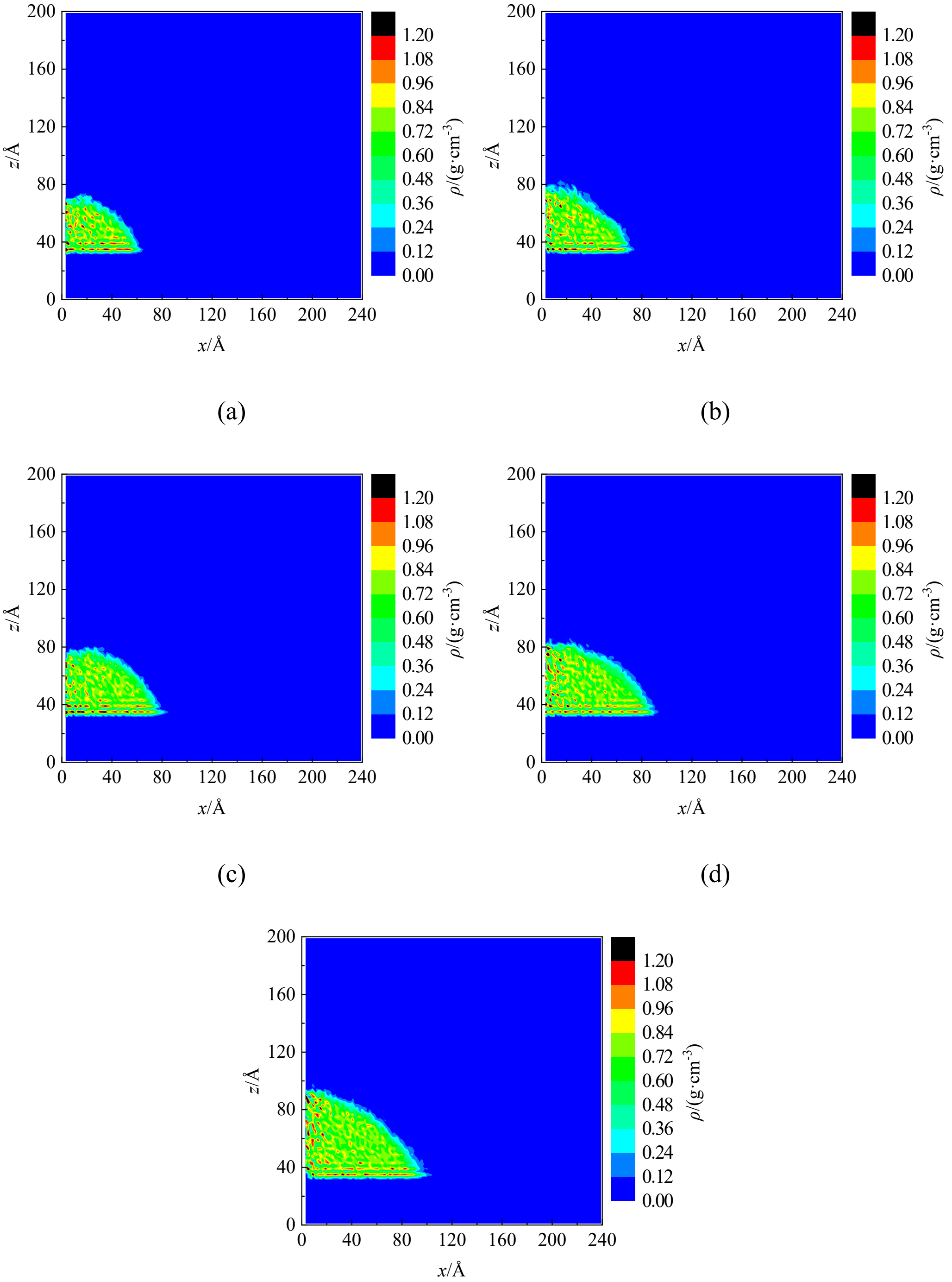

(a) (b)

(c) (d)

(e)

Fig. 5. Density profiles of the droplets with diameters of (a) 80 Å, (b) 90 Å, (c) 100 Å, (d) 110 Å and (e) 120 Å.

It can be seen from Fig. 4 and Fig. 5 that when the solid-liquid interaction coefficient is ε_2, the shapes of the droplets with different diameters on the smooth surfaces are similar and are all coronal. This indicates that the droplets with different diameters have small difference in shape when they reach the equilibrium states, that is, the influence of the droplet diameter on the shape of the equilibrium droplet is small.

At a solid-liquid interaction coefficient of ε_2, the density profile along the centerline of n-hexadecane droplet with a diameter of 100 Å on the SS at 2 ns is described in Fig. 6.

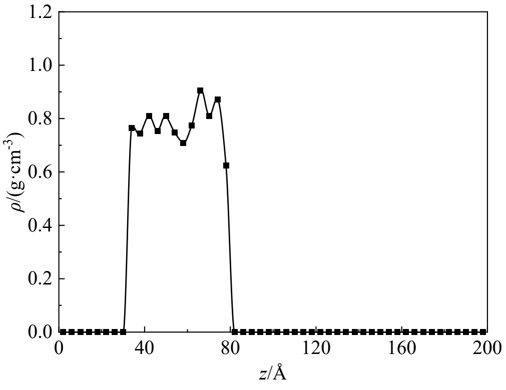

Fig. 6. Density profile of the droplet with a diameter of 100 Å.

As shown in Fig. 6, near the solid surface, the density fluctuation is large because of the presence of the wall. The density fluctuation inside the droplet is small, and the average value of the density of the droplet is calculated to be 0.7772 g/cm^3, which is very close to the density of n-hexadecane at room temperature. The above results verify the accuracy of the simulation processes. As the distance from the solid surface increases, the density decreases sharply and a liquid-vapor interface is formed. When the distance from the solid surface further increases, a vapor phase region is formed.

For the wetting processes of the droplets on the smooth surfaces, the variations of the *z*-coordinates of the mass centroids of the droplets with different diameters over time are compared as shown in Fig. 7.

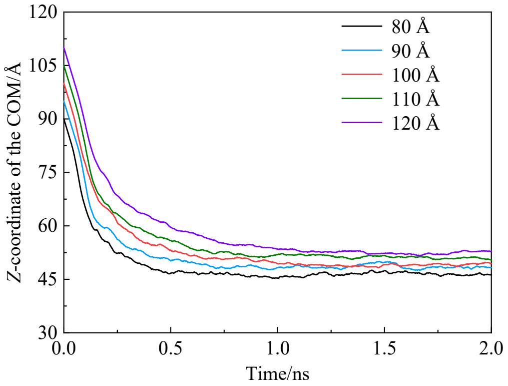

Fig. 7. Effects of the droplet diameter on the *z*-coordinates of the mass centroids of the droplets.

It can be seen from Fig. 7 that the *z*-coordinates of the mass centroids decrease rapidly when the droplets with different diameters wet the smooth surfaces. When the droplet reaches an equilibrium state, the changes in the *z*-coordinate of the mass centroid turn small. As the droplet diameter increases, the time it takes for the droplet to reach an equilibrium state is longer. After the droplet reaches an equilibrium state, it shows that the *z*-coordinate of the mass centroid slightly increases with increasing droplet diameter at the same time.

After calculations, the intrinsic CAs of the droplets with different diameters on the smooth surfaces are shown in Fig. 8.

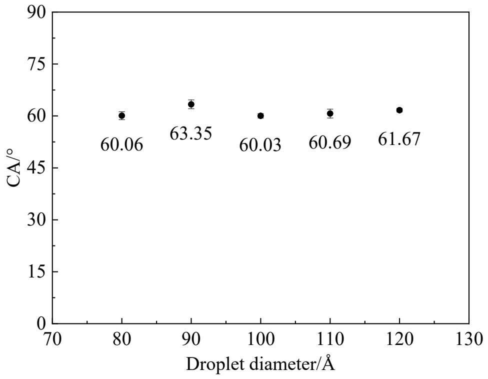

Fig. 8. Effects of the droplet diameter on the intrinsic CAs.

It can be seen from Fig. 8 that under the same solid-liquid interaction coefficient, the intrinsic CA of the droplet on the SS increases by 3.29° when the droplet diameter increases from 80 Å to 90 Å. When the droplet diameter further increases to 100 Å, 110 Å and 120 Å, the difference in the intrinsic CA of the droplet on the SS is less than 3°. It can be concluded that when the droplet diameter increases to 100 Å and above, the influence of the droplet diameter on the intrinsic CA is small. Therefore, considering the accuracy and efficiency of the calculations, in the follow-up simulations, the diameter of the droplet is selected to be 100 Å.

3.2. Analysis of the effects of the cutoff radius on the static wetting behaviors of the droplets

The cutoff radius of the Lennard-Jones potential affects the simulation results. To determine a reasonable cutoff radius, it is necessary to study the effects of the cutoff radius on the static wetting behaviors of the droplets. When the solid-liquid interaction coefficient is ε_2, under the conditions of the cutoff radii of 8 Å, 10 Å, 12 Å, 14 Å and 16 Å, the processes of n-hexadecane droplets with a diameter of 10 nm wetting a smooth surface are simulated. At a solid-liquid interaction coefficient of ε_2, under different cutoff radii, the snapshots and density profiles of the droplets on the smooth surfaces at 2 ns are shown in Fig. 9 and Fig. 10, respectively.

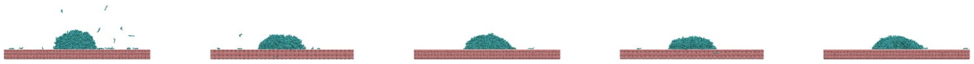

(a) (b) (c) (d) (e)

Fig. 9. Snapshots of the droplets on the smooth surfaces under cutoff radii of (a) 8 Å, (b) 10 Å, (c) 12 Å, (d) 14 Å and (e) 16 Å.

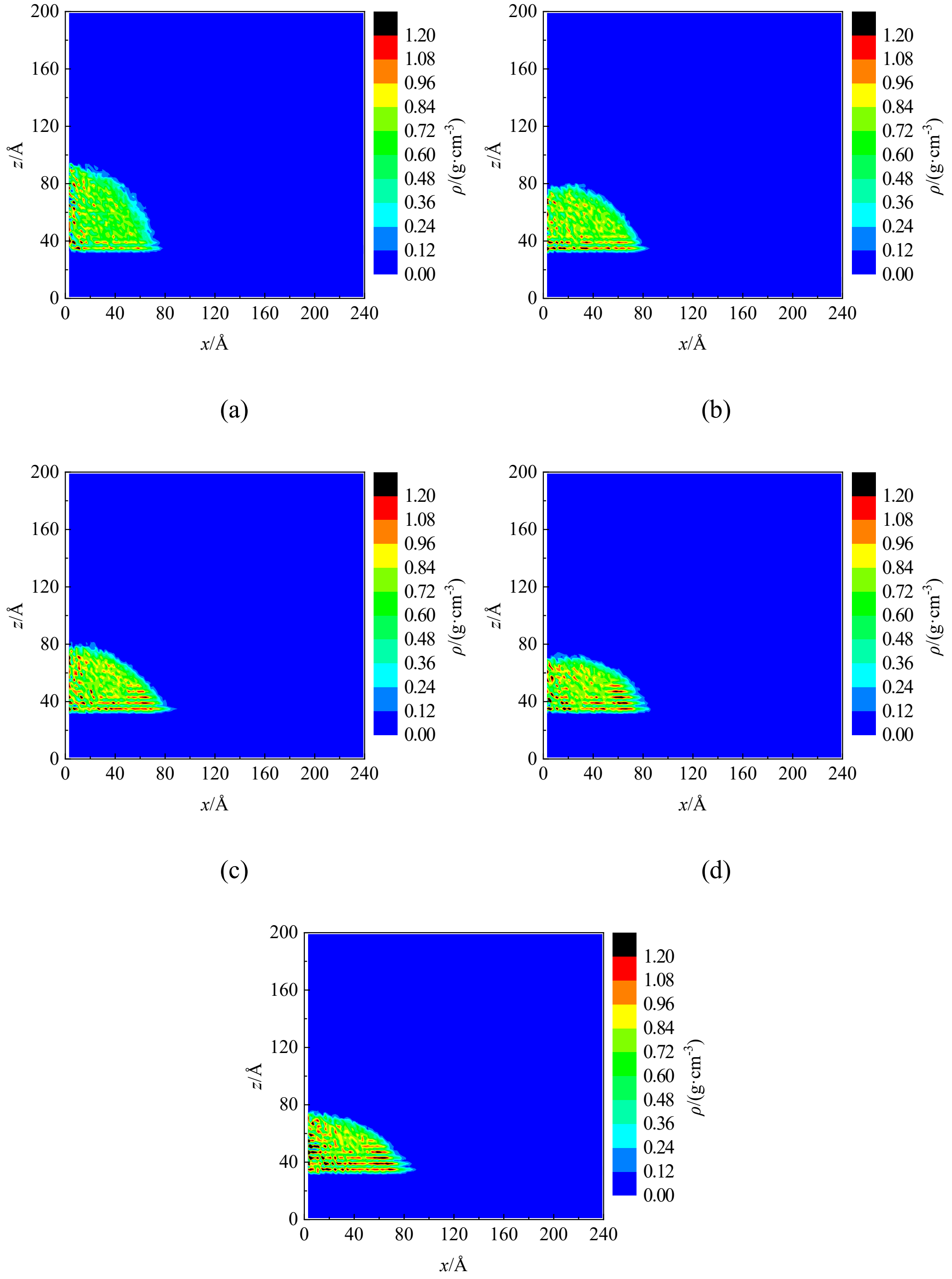

(a) (b)

(c) (d)

(e)

Fig. 10. Density profiles of the droplets on the smooth surfaces under cutoff radii of (a) 8 Å, (b) 10

Å, (c) 12 Å, (d) 14 Å and (e) 16 Å.

As seen in Fig. 9 and Fig. 10, at a solid-liquid interaction coefficient of ε_2, when the cutoff radius increases from 8 Å to 10 Å, the wetting ability of the droplet to the wall is enhanced. This is because the number of atoms within the cutoff radius increases with the increase of the cutoff radius, making the interaction between the wall and the droplet stronger. As the cutoff radius further increases to 12 Å, 14 Å and 16 Å, the shape of the droplet does not change significantly when it reaches an equilibrium state, that is, the influence of the cutoff radius on the shape of the equilibrium droplet is small.

When the solid-liquid interaction coefficient is ε_2, the influence of the cutoff radius on the *z*-coordinates of the mass centroids of the droplets is shown in Fig. 11.

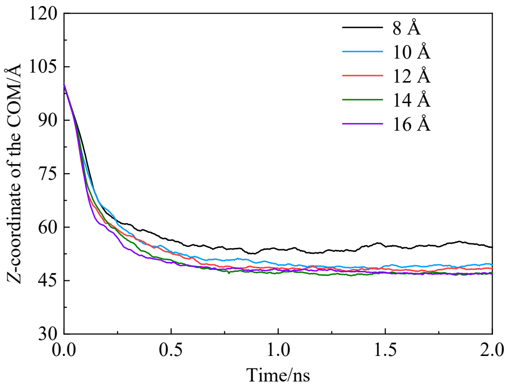

Fig. 11. Effects of the cutoff radius on the *z*-coordinates of the mass centroids of the droplets.

It can be seen from Fig. 10 that at a solid-liquid interaction coefficient of ε_2, when the cutoff radius rises from 8 Å to 10 Å, the *z*-coordinate of the mass centroid of the droplet in an equilibrium state reduces. As the cutoff radius further rises to 12 Å, 14 Å and 16 Å, the changes of the *z*-coordinate of the mass centroid of an equilibrium droplet become smaller. It can be concluded that after the cutoff radius reaches 10 Å, the cutoff radius has small effects on the *z*-coordinate of the COM.

When the solid-liquid interaction coefficient is ε_2, the intrinsic CAs of the droplets on the smooth surfaces under different cutoff radii are shown in Fig. 12.

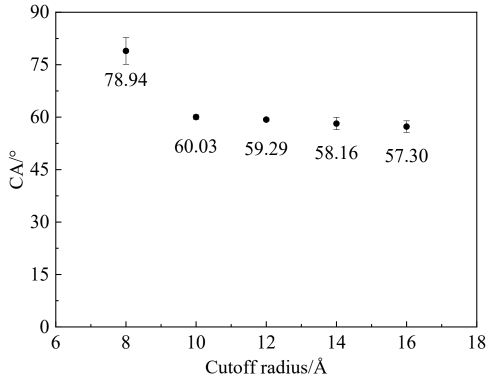

Fig. 12. Effects of the cutoff radius on the intrinsic CAs.

It can be seen from Fig. 12 that the intrinsic CA of the droplet on the SS decreases continuously with the increase of the cutoff radius. This is because the larger the cutoff radius, the stronger the wetting ability of the droplet to the wall and the smaller the intrinsic CA. When the cutoff radius is 8 Å, the intrinsic CA of the droplet on the SS is 78.94°. When the cutoff radius increases to 10 Å, the intrinsic CA is 60.03°, which decreases by 18.91°. Compared with the cutoff radius of 10 Å, when the cutoff radius further increases to 12 Å, 14 Å and 16 Å, the intrinsic CA of the droplet in an equilibrium state decreases slightly, being 59.29°, 58.16°, 57.30°, respectively. It can be concluded that the cutoff radius has small effects on the intrinsic CA. As a result, in the subsequent simulations of this study, the cutoff radius is selected to be 10 Å.

3.3. Analysis of the effects of the rough structure on the static wetting behaviors of the droplets

To deeply study the effects of the rough structure on the static wetting behaviors of the droplets, the static wetting processes of the droplets on the surfaces with different structures are simulated under the conditions of four solid-liquid interaction coefficients. The values of the roughness factor (r_s) of the surfaces with different structures and the ratio of the solid-liquid contact area to the composite contact area (f_1) are shown in Table 6.

Table 6. Values of r_s and f_1 of the surfaces with different rough structures.

	BS	PS	GS	DS
r_s	2	2	3	9/4
f_1	1/4	3/4	1/2	1/16

Under the conditions of four different solid-liquid interaction coefficients of ε_1, ε_2, ε_3 and ε_4, the snapshots of n-hexadecane droplets on different surfaces at 2 ns are shown in Fig. 13.

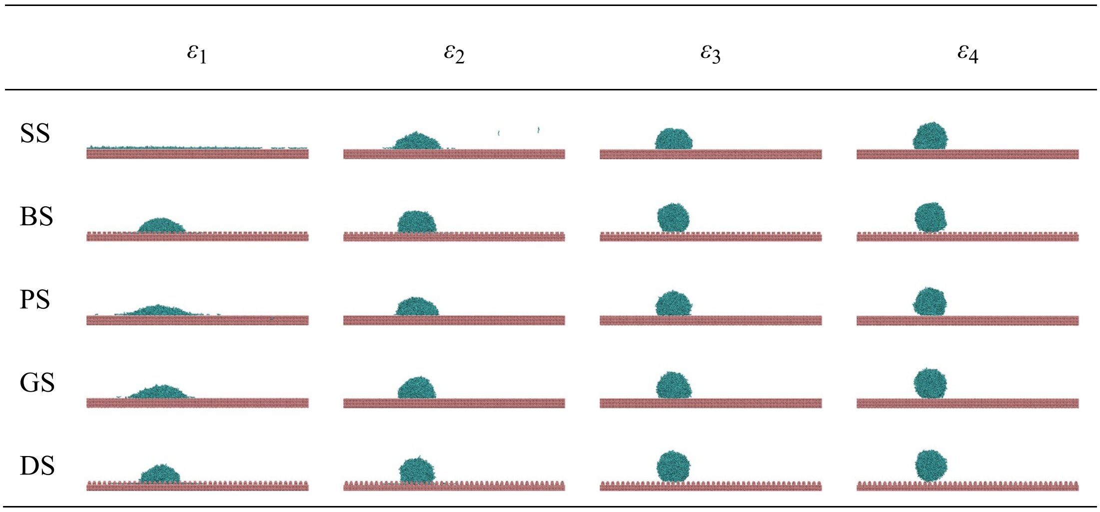

Fig. 13. Snapshots of the droplets on different surfaces.

In the simulation processes, it is found that when the solid-liquid interaction coefficient is ε_1, the droplet rapidly spreads after contacting the smooth surface, and the solid-liquid-vapor contact line rapidly expands. It can be seen from Fig. 13 that a precursor film appears during the spreading process of the droplet on the PS. With the decrease of the solid-liquid interaction coefficient, the three-phase contact lines on different surfaces retract. Compared with the smooth surfaces, the rough structures of other surfaces have an inhibitory effect on the spreading of the droplets. As the solid-liquid interaction coefficient decreases, the interaction between the wall and the droplet is weakened, and the wetting state changes from the Wenzel state to the Cassie state. On the BS, when the solid-liquid interaction coefficient decreases from ε_2 to ε_3, the wetting state changes from the Wenzel state to the Cassie state. For the Cassie state, the droplet in an equilibrium state is supported by the top of the rough structures, and the bottom of the droplet only contacts the top of the bosses of the surface without infiltrating into the pits. In addition, as the ratio of the solid-liquid contact area to the composite contact area decreases, it is easier for the droplet to reach the Cassie state.

Under different solid-liquid interaction coefficients, the variations of the energy between the droplets and the walls (E_{DW}) with time are shown in Fig. 14.

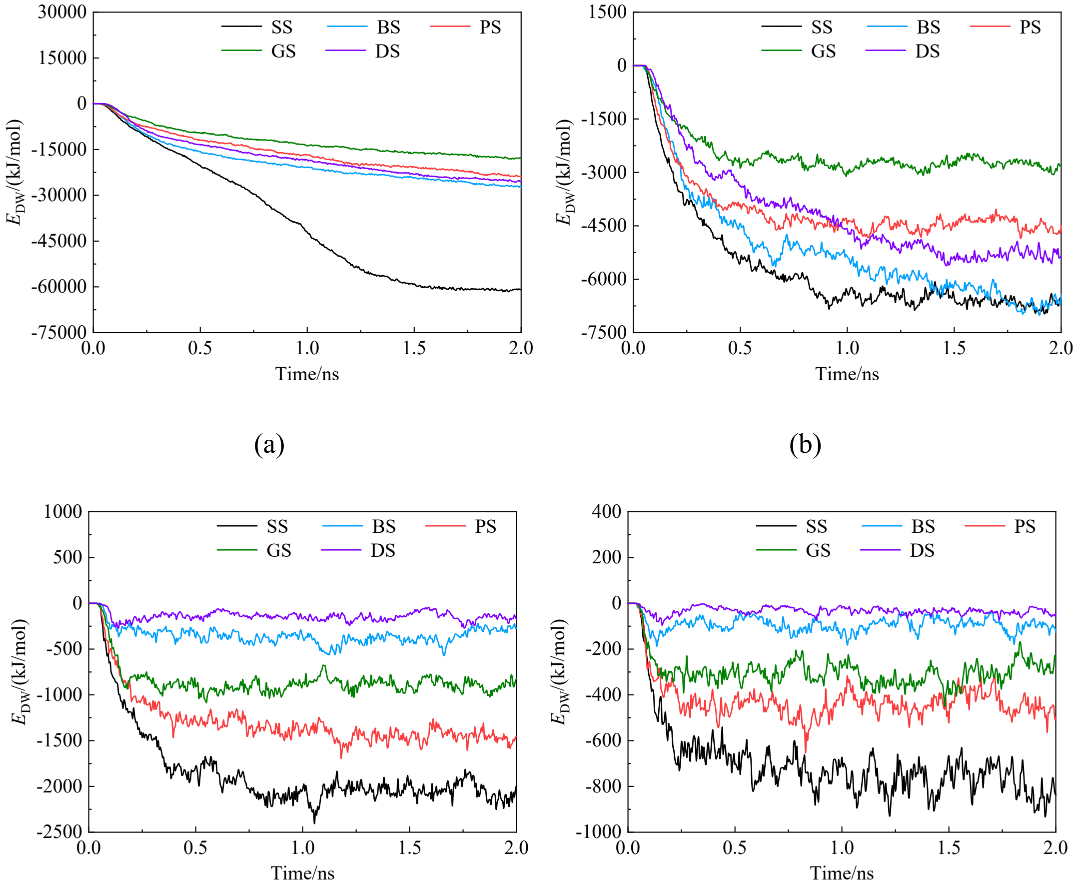

(a) (b)

(c) (d)

Fig. 14. Variations of E_{DW} with time under the solid-liquid interaction coefficients of (a) ε_1, (b) ε_2, (c) ε_3 and (d) ε_4.

It can be seen from Fig. 14 that the interaction forces between different walls and the droplets are all attractive forces. On the same surface, as the solid-liquid interaction coefficient decreases, the interaction between the wall and the droplet is significantly weakened, and the inflection point of the time when the E_{DW} tends to be stable appears earlier. When the solid-liquid interaction coefficient is high, the interaction between the solid surface and the droplet is strong, so the droplet on the surface needs to be stable after a while. However, when the solid-liquid interaction coefficient is low, the interaction strength is weak, the wetting behaviors of the droplet on the surface are mainly affected by the force of the droplet molecules themselves, and the droplet tends to be stable in a short time. Under the same solid-liquid interaction coefficient, compared with the surfaces with different structures, the interaction between the smooth surface and the droplet is the strongest due to the largest contact area between the smooth surface and the droplet.

Under different solid-liquid interaction coefficients, the intrinsic CAs of n-hexadecane droplets on the smooth surfaces and the apparent CAs on the surfaces with different structures are shown in Fig. 15.

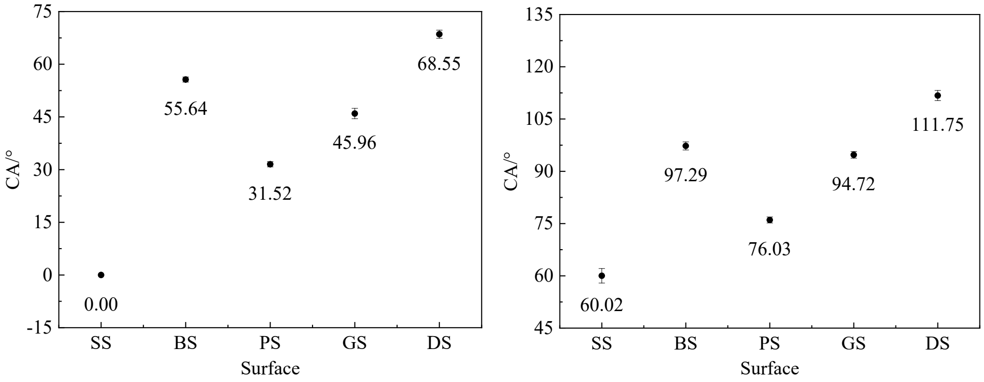

(a) (b)

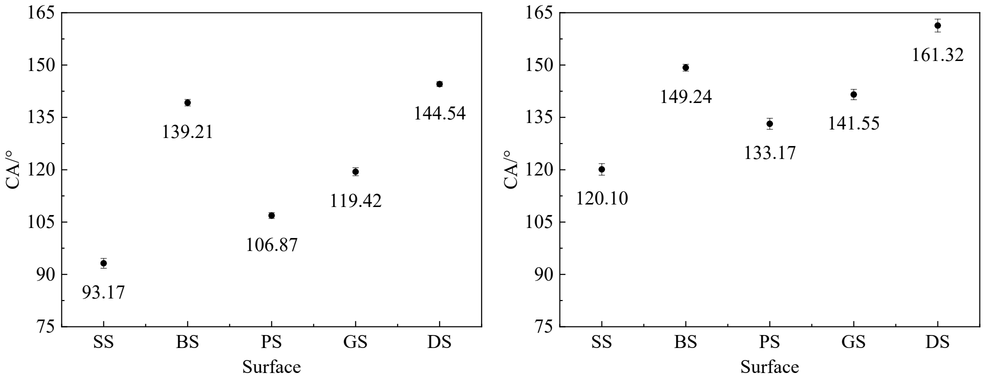

(c) (d)

Fig. 15. Static CAs of the droplets on different surfaces under the solid-liquid interaction coefficients of (a) ε_1, (b) ε_2, (c) ε_3 and (d) ε_4.

As can be seen in Fig. 15, under the conditions of four solid-liquid interaction coefficients of ε_1, ε_2, ε_3 and ε_4, the intrinsic CAs of n-hexadecane droplets on the smooth surfaces are 0°, 60.02°, 93.17° and 120.10°, respectively, which means that under the above solid-liquid interaction coefficients, the surfaces are superoleophilic, oleophilic, neutral and oleophobic in turn. The CA linearly increases with the decrease of the solid-liquid interaction coefficient. The main reason for the above results is that with the decrease of the solid-liquid interaction coefficient, the interaction between the wall and the droplet is weakened, and the tendency of the droplet molecules to move closer to the wall is weakened, which reduces the number of droplet molecules attracted to the wall, resulting in an increase in the intrinsic CA.

Under the conditions of ε_1, ε_2, ε_3 and ε_4, the apparent CAs of n-hexadecane droplets on the surfaces with different structures are all larger than their intrinsic CAs on the smooth surfaces. Taking ε_2 as an example, the intrinsic CA of n-hexadecane droplet on the SS is 60.02°, and the apparent CAs on the BS, PS, GS and DS are 97.29°, 76.03°, 94.72° and 111.75°, respectively. The apparent CA on the DS increases by 51.73° compared to the intrinsic CA on the SS. It can be concluded that the rough structures of the surfaces are beneficial to enhance the oleophobicity of the surfaces, especially the secondary boss-shaped structures can significantly enhance the oleophobicity. This is because the rough microstructures of the surfaces hinder the spreading processes of the droplets on the surfaces. Compared with the BS, PS and GS, the value of f_1 of the DS is the smallest. That means, in the composite contact area, the proportion of the solid-liquid contact area of the DS is the smallest, and the proportion of the liquid-vapor contact area of it is the largest. It can be inferred that the ability of the secondary boss-shaped structures to capture air is stronger, which leads to the largest CA on the DS. According to the above results, when the thermal atmosphere in the engine cylinder is poor and the wall temperature is low, increasing the oleophobicity of the cylinder walls in the areas with a high probability of being hit by the fuel droplets through constructing the secondary structures is conducive to the rebound of the droplets, thereby promoting the evaporation of the droplets in the gas-phase space of the cylinder and improving the atomization quality.

3.4. Analysis of the effects of the rough structure on the dynamic wetting behaviors of the droplets

To simulate the dynamic wetting processes of the droplets in the equilibrium states on different surfaces under various solid-liquid interaction coefficients, an external force is applied to them. The values of the external forces exerted on the atoms CH_3 and CH_2 under the four solid-liquid interaction coefficients are shown in Table 7.

Table 7. Values of the external forces applied to atoms CH_3 and CH_2.

	ε_1	ε_2	ε_3	ε_4
F_{CH_3}/kJ·mol^{-1}·Å^{-1}	0.008969	0.004485	0.002242	0.001121

F_{CH_2}/kJ·mol^{-1}·Å^{-1}	0.008368	0.004184	0.002092	0.001046

The snapshots of n-hexadecane droplets on different surfaces at 0.5 ns after the external force is applied are shown in Fig. 16.

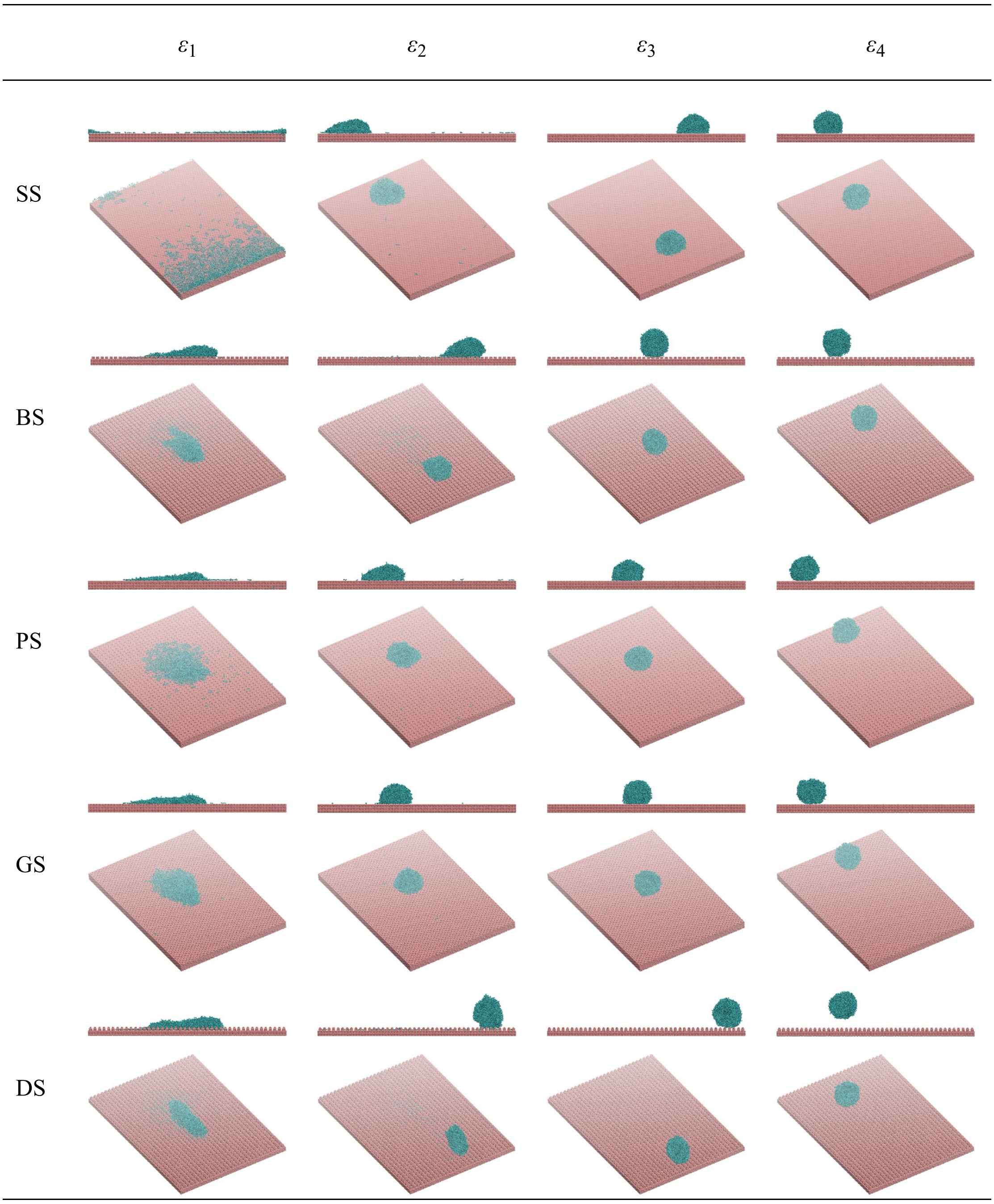

Fig. 16. Snapshots of the dynamic wetting processes of the droplets on different surfaces.

As can be seen in Fig. 16, under different solid-liquid interaction coefficients, the morphologies of the droplets during the lateral movements on different surfaces can be mainly classified into three categories: being continuously stretched, being considerably distorted and maintaining the initial shape. The simulation results are similar to those of Jeong et al. (2012). During the simulations, it was found that the droplet gained a velocity in the positive x direction under the action of the external force. However, due to the external force and the pinning effect of the wall on the droplet, the droplet molecules generate a velocity gradient, which leads to the deformation of the droplet. Furthermore, it is found that the droplet moves on the surface in a rolling manner rather than in a translational manner. As can be seen in Fig. 16, when the solid-liquid interaction coefficient is ε_1, the droplets infiltrate into the pits of the walls and are in a Wenzel state on different surfaces. As a result, the micro rough structures of the surfaces have significant effects on the lateral movements of the droplets. Due to the large difference in the moving speed of the droplet molecules, the droplet is greatly stretched in the x-axis direction. At ε_2, the droplets are still in a Wenzel state on the SS, BS, PS and GS under the action of external force, and their shapes become asymmetrical. However, the droplet on the DS is in a Cassie state, and its shape does not significantly change. When the solid-liquid interaction coefficients are ε_3 and ε_4, under the action of the external force, the droplets are in a Cassie state on all different surfaces, and there are slight variations in their contours.

To quantify the effects of the solid-liquid interaction coefficient and structure on the dynamic wetting processes of the droplets, the advancing contact angle (ACA), receding contact angle (RCA) and contact angle hysteresis (CAH) are calculated. The results are shown in Fig. 17.

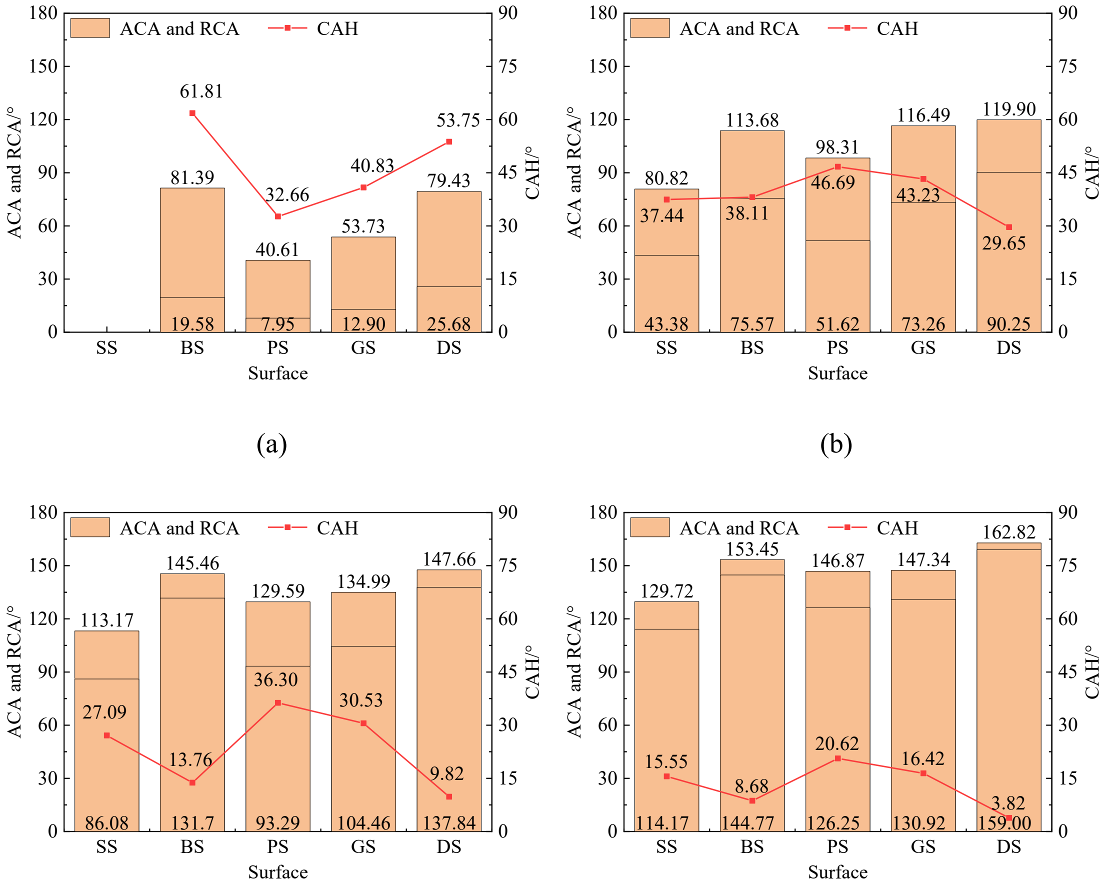

(a) (b)

(c) (d)

Fig. 17. Dynamic CAs of the droplets on different surfaces under the solid-liquid interaction coefficients of (a) ε_1, (b) ε_2, (c) ε_3 and (d) ε_4.

As shown in Fig. 17, at a solid-liquid interaction coefficient of ε_1, the receding contact angles of the droplets on the four rough surfaces are small. This is mainly because, as mentioned in the previous section, when the solid-liquid interaction coefficient is ε_1, the Wenzel state is maintained during the movements of the droplets on all the surfaces with different structures, and the droplets are stretched on different surfaces. It should be noted that since the droplet on the SS is greatly stretched to form a thin liquid film, the ACA, RCA and CAH on the SS are not given in Fig. 17(a). When the solid-liquid interaction coefficients are ε_2, ε_3 and ε_4, the effects of the rough structure on the CAH mainly include two aspects. On the one hand, compared with the smooth surfaces, the rough structures hinder the movements of the droplets, resulting in an increase in the CAH. On the other hand, the rough structures can enhance the surface oleophobicity compared with the smooth surfaces, leading to a decrease in the CAH. For example, for the PS, the former plays a major role. As a result, the CAH on the PS is larger than that on the SS. As shown in Figures 17(b), 17(c) and 17(d), among the four rough surfaces, the CAH of the droplet on the PS is the largest, and the CAH is 46.69°, 36.30° and 20.62°, respectively. The main reason for the above results is that the value of f_1 of the PS is the largest among the four rough surfaces, which makes the interaction between the surface and the droplet the strongest, resulting in the highest potential barrier that needs to be overcome during the movement of the droplet. In addition, at the solid-liquid interaction coefficients of ε_2, ε_3 and ε_4, on the four rough surfaces, the CAH on the DS is the smallest, which is 29.65°, 9.82° and 3.82°, respectively. This is related to the strongest oleophobicity of the DS resulting from the smallest value of f_1 among the four rough surfaces. Also, the CAH of the droplets on the DS is 7.79°, 17.27° and 11.73° lower than that on the SS. The above results show that the secondary boss-shaped structures can significantly enhance the oleophobicity of the surface, which is consistent with the previous conclusion.

As the solid-liquid interaction coefficient decreases from ε_2 to ε_4, the pinning effect is weakened, so the binding effect of the wall atoms to the droplet molecules near the solid surface becomes weaker, which reduces the number of slow-moving droplet molecules near the solid surface. As a result, the CAH of the droplets on different surfaces continuously decreases with the decrease of the solid-liquid interaction coefficient. At the same time, the interaction between the wall atoms and the molecules in the middle and upper parts of the droplet is weakened, so the resistance to movement during the dynamic wetting process reduces. Also, because there is a small velocity gradient between the molecules of each layer of the droplet, the change degree in the shape of the droplet reduces, which reduces the variations of the ACA and RCA relative to the apparent CA. Therefore, the CAH reduces. Compared with the Wenzel state, since the droplet in the Cassie state is in contact with the upper parts of the rough structures and does not infiltrate into the pits of the structures, the movement of the droplet is not significantly hindered by the rough structures. In addition, when the droplet is in the Cassie state, the actual contact area between the wall and the droplet is small, which makes the interaction between the wall and the droplet weak, resulting in low resistance during the lateral movement process. Therefore, the CAH of a droplet in the Cassie state is smaller than that of a droplet in the Wenzel state.

4. Conclusion

The molecular dynamics method is used to simulate the static and dynamic wetting behaviors of the droplets on different surfaces. The influence of the droplet diameter on the intrinsic CA is analyzed. The effects of the solid-liquid interaction coefficient and rough structures on the apparent CA and the CAH are revealed. The main conclusions are as follows:

(1) Under the condition of the same solid-liquid interaction coefficient, after the droplets with different diameters reach the equilibrium states on the smooth surfaces, the variations of the z-coordinates of the mass centroids are small. As the droplet diameter increases, it takes longer for the droplet to reach an equilibrium state, and the z-coordinate of the mass centroid after reaching the equilibrium state slightly increases. The droplet diameter has little influence on the intrinsic CA.

(2) At a solid-liquid interaction coefficient of ε_2, as the cutoff radius increases, the interaction between the wall and the droplet is enhanced, so the wetting ability of the droplet to the wall is enhanced, the z-coordinate of the mass centroid of the droplet in an equilibrium state decreases, and

the intrinsic CA reduces. As the cutoff radius further increases from 1.0 nm to 1.2 nm, 1.4 nm and 1.6 nm, the effects of the cutoff radius on the shape, the *z*-coordinate of the mass centroid and the intrinsic CA of an equilibrium droplet are small.

(3) Compared with the smooth surfaces, the rough structures of the surfaces have an inhibitory effect on the spreading of the droplets. As the solid-liquid interaction coefficient decreases, the interaction between the wall and the droplet is weakened, and the wetting state changes from the Wenzel state to the Cassie state. As the ratio of the solid-liquid contact area to the composite contact area decreases, it is easier for the droplet to reach the Cassie state.

(4) Under the conditions of four solid-liquid interaction coefficients of ε_1, ε_2, ε_3 and ε_4, the intrinsic CAs of the droplets on the smooth surfaces are 0°, 60.02°, 93.17° and 120.10°, respectively. The apparent CAs of the droplets on the surfaces with different structures are all larger than their intrinsic CAs on the smooth surfaces. At a solid-liquid interaction coefficient of ε_2, the apparent CA on the surface with the secondary boss-shaped structures increases by 51.73° compared to the intrinsic CA on the smooth surface. It can be concluded that the secondary boss-shaped structures can effectively enhance the surface oleophobicity.

(5) Under the action of the external force, the velocities of all the droplet molecules are not the same, resulting in a velocity gradient, which changes the shape of the droplet. Furthermore, the droplet moves on the surface in a rolling manner rather than in a translational manner. The decrease in the solid-liquid interaction coefficient weakens the pinning effect of the wall on the droplet, resulting in a lower CAH. The CAH significantly decreases when the droplet transitions from the Wenzel state to the Cassie state.

CRediT authorship contribution statement

Yanling Chen: Conceptualization, Data curation, Formal analysis, Investigation, Methodology, Software, Writing – original draft. **Liang Guo:** Formal analysis, Funding acquisition, Validation, Writing – review & editing. **Wanchen Sun:** Formal analysis, Supervision, Validation. **Ningning Cai:** Writing – review & editing. **Yuying Yan:** Supervision, Validation.

Declaration of competing interest

The authors declare that they have no known competing financial interests or personal relationships that could have appeared to influence the work reported in this paper.

Data availability

Data will be made available on request.

Acknowledgments

The authors gratefully acknowledge the financial support from the Natural Science Foundation of Jilin Province (Project code: 20220101212JC), Jilin Province Specific Project of Industrial Technology Research & Development (Project code: 2020C025-2), Free Exploration Project of Changsha Automotive Innovation Research Institute of Jilin University (Project code: CAIRIZT20220202), 2021 “Interdisciplinary Integration and Innovation” Project of Jilin University (Project code: XJRCYB07) and Horizon 2020 MSCA (Project code: H2020-MSCA-RISE-778104-ThermaSMART).

References

Abramov, A., Iglauer, S., 2019. Analysis of individual molecular dynamics snapshots simulating wetting of surfaces using spheroidal geometric constructions. J. Chem. Phys. 151 (6). https://doi.org/10.1063/1.5113852

Agarwal, A.K., Singh, A.P., Maurya, R.K., 2017. Evolution, challenges and path forward for low temperature combustion engines. Prog. Energy Combust. Sci. 61, 1-56. https://doi.org/10.1016/j.pecs.2017.02.001

Ambrosia, M.S., Ha, M.Y., Balachandar, S., 2013. The effect of pillar surface fraction and pillar height on contact angles using molecular dynamics. Appl. Surf. Sci. 282, 211-216. https://doi.org/10.1016/j.apsusc.2013.05.104

Bai, L., Wang B.H., Yu Z.J., 2017. Molecular dynamics simulation of wetting behavior of n-hexadecane nanodroplets on smooth surfaces. Henan Chemical Industry 34 (11), 25-29. https://doi.org/10.14173/j.cnki.hnhg.2017.11.005

Bendu, H., Murugan, S., 2014. Homogeneous charge compression ignition (HCCI) combustion: Mixture preparation and control strategies in diesel engines. Renew Sust Energ Rev 38, 732-746. https://doi.org/10.1016/j.rser.2014.07.019

Bhushan, B., Jung, Y.C., Koch, K., 2009. Self-cleaning efficiency of artificial superhydrophobic surfaces. Langmuir 25 (5), 3240-3248. https://doi.org/10.1021/la803860d

Bonometti, T., Magnaudet, J., 2007. An interface-capturing method for incompressible two-phase flows. Validation and application to bubble dynamics. Int. J. Multiphase Flow 33 (2), 109-133. https://doi.org/10.1016/j.ijmultiphaseflow.2006.07.003

Burt, R., Birkett, G., Salanne, M., Zhao, X.S., 2016. Molecular dynamics simulations of the influence of drop size and surface potential on the contact angle of ionic-liquid droplets. J. Phys. Chem. C 120 (28), 15244-15250. https://doi.org/10.1021/acs.jpcc.6b04696

Cassie, A.B.D., Baxter, S., 1944. Wettability of porous surfaces. Transactions of the Faraday Society 40 (1), 546-551. https://doi.org/10.1039/TF9444000546

Chen, S., Wang, J.D., Chen, D.R., 2014. States of a water droplet on nanostructured surfaces. J. Phys. Chem. C 118 (32), 18529-18536. https://doi.org/10.1021/jp504070e

Chen, S., Wang, J.D., Ma, T.B., Chen, D.R., 2014. Molecular dynamics simulations of wetting behavior of water droplets on polytetrafluorethylene surfaces. J. Chem. Phys. 140 (11). https://doi.org/10.1063/1.4868641

Chen, Y.L., Guo, L., Cai, N.N., Sun, W.C., Yan, Y.Y., Li, D.G., Wang, H., Xuan, R., 2023. Evaporation characteristics and morphological evolutions of fuel droplets after hitting different wettability surfaces. J Bionic Eng. 20 (2), 734-747. https://doi.org/10.1007/s42235-022-00293-y

Farhadi, S., Farzaneh, M., Kulinich, S.A., 2011. Anti-icing performance of superhydrophobic surfaces. Appl. Surf. Sci. 257 (14), 6264-6269. https://doi.org/10.1016/j.apsusc.2011.02.057

Gordon, D., Wouters, C., Kinoshita, S., Wick, M., Lehrheuer, B., Andert, J., Pischinger, S., Koch, C.R., 2020. Homogeneous charge compression ignition combustion stability improvement using a rapid ignition system. Int. J. Engine Res. 21 (10), 1846-1856. https://doi.org/10.1177/1468087420917769

Guo, H.K., Fang, H.P., 2005. Drop size dependence of the contact angle of nanodroplets. Chinese Physics Letters 22 (4), 787-790. https://doi.org/10.1088/0256-307X/22/4/002

Guo, L., Chen, Y.L., Cai, N.N., Sun, W.C., Yan, Y.Y., Wang, H., Gao, Y.H., 2022. Dynamic behaviors of fuel droplets impacting on the wall surfaces with different wettability and temperatures. Appl. Therm. Eng. 212. https://doi.org/10.1016/j.applthermaleng.2022.118536

Hong, S.D., Ha, M.Y., Balachandar, S., 2009. Static and dynamic contact angles of water droplet on a solid surface using molecular dynamics simulation. J. Colloid Interface Sci. 339 (1), 187-

195. https://doi.org/10.1016/j.jcis.2009.07.048

Jeong, W.J., Ha, M.Y., Yoon, H.S., Ambrosia, M., 2012. Dynamic behavior of water droplets on solid surfaces with pillar-type nanostructures. Langmuir 28 (12), 5360-5371. https://doi.org/10.1021/la205106v

Khalkhali, M., Kazemi, N., Zhang, H., Liu, Q.X., 2017. Wetting at the nanoscale: A molecular dynamics study. J. Chem. Phys. 146 (11). https://doi.org/10.1063/1.4978497

Kim, J.H., Mirzaei, A., Kim, H.W., Kim, S.S., 2018. Facile fabrication of superhydrophobic surfaces from austenitic stainless steel (AISI 304) by chemical etching. Appl. Surf. Sci. 439, 598-604. https://doi.org/10.1016/j.apsusc.2017.12.211

Koishi, T., Yasuoka, K., Fujikawa, S., Zeng, X.C., 2011. Measurement of contact-angle hysteresis for droplets on nanopillared surface and in the Cassie and Wenzel states: A molecular dynamics simulation study. Acs Nano 5 (9), 6834-6842. https://doi.org/10.1021/nn2005393

Krishnamoorthi, M., Malayalamurthi, R., He, Z.X., Kandasamy, S., 2019. A review on low temperature combustion engines: Performance, combustion and emission characteristics. Renew Sust Energ Rev 116. https://doi.org/10.1016/j.rser.2019.109404

Kwon, T.W., Lee, K.H., Seo, Y.M., Jang, J., Ha, M.Y., 2020. Dynamic wetting behaviors of water droplets on surfaces with dual structures at the nanoscale. Int. J. Multiphase Flow 129. https://doi.org/10.1016/j.ijmultiphaseflow.2020.103352

Lee, C.Y., Zhang, B.J., Park, J., Kim, K.J., 2012. Water droplet evaporation on Cu-based hydrophobic surfaces with nano- and micro-structures. Int. J. Heat Mass Transfer 55 (7-8), 2151-2159. https://doi.org/10.1016/j.ijheatmasstransfer.2011.12.019

Lee, J., Chu, S., Cha, J., Choi, H., Min, K., 2015. Effect of the diesel injection strategy on the combustion and emissions of propane/diesel dual fuel premixed charge compression ignition engines. Energy 93, 1041-1052. https://doi.org/10.1016/j.energy.2015.09.032

Li, S.H., Page, K., Sathasivam, S., Heale, F., He, G.J., Lu, Y., Lai, Y.K., Chen, G.Q., Carmalt, C.J., Parkin, I.P., 2018. Efficiently texturing hierarchical superhydrophobic fluoride-free translucent films by AACVD with excellent durability and self-cleaning ability. J. Mater. Chem. A 6 (36), 17633-17641. https://doi.org/10.1039/c8ta05402a

Liang, X.Y., Zheng, Z.W., Zhang, H.S., Wang, Y.S., Yu, H.Z.N., 2019. A review of early injection strategy in premixed combustion engines. Applied Sciences-Basel 9 (18). https://doi.org/10.3390/app9183737

Martines, E., Seunarine, K., Morgan, H., Gadegaard, N., Wilkinson, C.D.W., Riehle, M.O., 2005. Superhydrophobicity and superhydrophilicity of regular nanopatterns. Nano Lett. 5 (10), 2097-2103. https://doi.org/10.1021/nl051435t

Mathivanan, K., Mallikarjuna, J.M., Ramesh, A., 2016. Influence of multiple fuel injection strategies on performance and combustion characteristics of a diesel fuelled HCCI engine - An experimental investigation. Exp. Therm Fluid Sci. 77, 337-346. https://doi.org/10.1016/j.expthermflusci.2016.05.010

Niu, D., Tang, G.H., 2014. Static and dynamic behavior of water droplet on solid surfaces with pillar-type nanostructures from molecular dynamics simulation. Int. J. Heat Mass Transfer 79, 647-654. https://doi.org/10.1016/j.ijheatmasstransfer.2014.08.047

Ou, J., Perot, B., Rothstein, J.P., 2004. Laminar drag reduction in microchannels using ultrahydrophobic surfaces. Phys. Fluids 16 (12), 4635-4643. https://doi.org/10.1063/1.1812011

Plimpton, S., 1995. Fast parallel algorithms for short-range molecular dynamics. J. Comput. Phys. 117(1), 1-19. https://doi.org/10.1006/jcph.1995.1039

Qi, C.H., Chen, H., Shen, L.Y., Li, X.L., Fu, Q., Zhang, Y.H., Sun, Y.Y., Liu, Y.Q., 2020. Superhydrophobic surface based on assembly of nanoparticles for application in anti-icing under ultralow temperature. ACS Appl. Nano Mater 3 (2), 2047-2057. https://doi.org/10.1021/acsanm.0c00220

Qian, H.C., Xu, D.K., Du, C.W., Zhang, D.W., Li, X.G., Huang, L.Y., Deng, L.P., Tu, Y.C., Mol, J.M.C., Terryn, H.A., 2017. Dual-action smart coatings with a self-healing superhydrophobic surface and anti-corrosion properties. J. Mater. Chem. A 5 (5), 2355-2364. https://doi.org/10.1039/c6ta10903a

Ravipati, S., Aymard, B., Kalliadasis, S., Galindo, A., 2018. On the equilibrium contact angle of sessile liquid drops from molecular dynamics simulations. J. Chem. Phys. 148 (16). https://doi.org/10.1063/1.5021088

Saleh, T.A., Baig, N., 2019. Efficient chemical etching procedure for the generation of superhydrophobic surfaces for separation of oil from water. Prog. Org. Coat. 133, 27-32. https://doi.org/10.1016/j.porgcoat.2019.03.049

Sankaralingam, R.K., Feroskhan, M., Elango, M., Khan, T.M.Y., Javed, S., Baig, R.U., Thangavel, V., 2022. Experimental studies on premixed charge and reactivity-controlled compression ignition combustion modes using gasoline/diesel fuel combination. Case Stud. Therm. Eng. 39. https://doi.org/10.1016/j.csite.2022.102467

Song, D., Song, B.W., Hu, H.B., Du, X.S., Ma, Z.B., 2015. Contact angle and impinging process of droplets on partially grooved hydrophobic surfaces. Appl. Therm. Eng. 85, 356-364.

https://doi.org/10.1016/j.applthermaleng.2015.03.071

Taghvaei, E., Moosavi, A., Nouri-Borujerdi, A., Daeian, M.A., Vafaeinejad, S., 2017. Superhydrophobic surfaces with a dual-layer micro- and nanoparticle coating for drag reduction. Energy 125, 1-10. https://doi.org/10.1016/j.energy.2017.02.117

Wenzel, R.N., 1936. Resistance of solid surfaces to wetting by water. Industrial and Engineering Chemistry 28 (8), 988-994. https://doi.org/10.1021/ie50320a024

Xin, G.Q., Wu, C.Y., Liu, W.N., Rong, Y.M., Huang, Y., 2021. Anti-corrosion superhydrophobic surfaces of Al alloy based on micro-protrusion array structure fabricated by laser direct writing. J. Alloys Compd. 881. https://doi.org/10.1016/j.jallcom.2021.160649

Yao, C.W., Tang, S.R., Sebastian, D., Tadmor, R., 2020. Sliding of water droplets on micropillar-structured superhydrophobic surfaces. Appl. Surf. Sci. 504. https://doi.org/10.1016/j.apsusc.2019.144493

Yong, J.L., Chen, F., Yang, Q., Hou, X., 2015. Femtosecond laser controlled wettability of solid surfaces. Soft Matter 11 (46), 8897-8906. https://doi.org/10.1039/c5sm02153g

Yoshimitsu, Z., Nakajima, A., Watanabe, T., Hashimoto, K., 2002. Effects of surface structure on the hydrophobicity and sliding behavior of water droplets. Langmuir 18 (15), 5818-5822. https://doi.org/10.1021/la020088p

Young, T., 1805. An essay on the cohesion of fluids. Philosophical Transactions of the Royal Society of London 95, 65-87. https://doi.org/10.1098/rstl.1805.0005

Yu, D.I., Kwak, H.J., Doh, S.W., Kang, H.C., Ahn, H.S., Kiyofumi, M., Park, H.S., Kim, M.H., 2015. Wetting and evaporation phenomena of water droplets on textured surfaces. Int. J. Heat Mass Transfer 90, 191-200. https://doi.org/10.1016/j.ijheatmasstransfer.2015.06.046

Zhang, Z.Q., Matin, M.A., Ha, M.Y., Jang, J., 2016. Molecular dynamics study of the hydrophilic-to-hydrophobic switching in the wettability of a gold surface corrugated with spherical cavities. Langmuir 32 (37), 9658-9663. https://doi.org/10.1021/acs.langmuir.6b02378

Zielkiewicz, J., 2005. Structural properties of water: Comparison of the SPC, SPCE, TIP4P, and TIP5P models of water. J. Chem. Phys. 123 (10). https://doi.org/10.1063/1.2018637